Dynamic Compression-shear Response of Brittle Materials with Specimen Recovery

by H. D. Espinosa, A. Patanella and Y. Xu

ABSTRACT—A new configuration for compression-shear soft-recovery experiments is presented. This technique is used to investigate various failure mechanisms during dynamic multiaxial loading of an Al_2O_3/SiC nanocomposite and TiB_2. Velocity profiles of the target surface are measured with a variable sensitivity displacement interferometer, yielding normal and transverse velocity-time histories. A dynamic shear stress of approximately 280 MPa is obtained, in the Al_2O_3/SiC nanocomposite, for an imposed axial stress of about 3.45 GPa on a 540 μm thick sample. This dynamic shear stress is well below the value predicted by elastic wave propagation theory. This could be the result of stress-induced damage and inelasticity in the bulk of the sample or inelasticity on the sample surface due to frictional sliding. To gain further insight into the possible failure mechanisms, an investigation of compression-shear recovery techniques, with simultaneous trapping of longitudinal and lateral release waves, is conducted.

KEY WORDS—Fragmentation, damage, ceramics, impact, wave propagation, nanocomposites

Normal impact soft-recovery experiments have been used in the past to study crystal plasticity[1] and microcracking in brittle materials.[2–5] In these experiments, a star-shaped flyer impacts a square specimen backed by another square plate called a momentum trap. Well-defined short duration axial stress pulses followed by a controlled release of waves were achieved. The main idea in this configuration is to keep a central octagonal region of the specimen plate relatively free from the effects of lateral unloading waves. Cylindrical, spherical and conical waves are generated at the flyer boundary (for a detailed discussion, see Ref. 1), directing most of the energy associated with the side rarefactions to regions at the periphery of the target plate and, hence, away from its center.

Chang *et al.*[6] further investigated the effect of flyer plate thickness and shape on the stress history within the specimen. They observed that tensile cracks form, normal to the free edges of brittle square specimens, when a thick, 2 mm to 4 mm star-shaped flyer is used. By means of three-dimensional numerical simulations, Chang *et al.* showed that in-plane tensile stresses are induced, on the back face of the sample, that could lead to the formation of cross-shaped cracks. This effect was attributed to the size mismatch between the flyer and the sample. As an improvement, Chang *et al.* recommended the use of side momentum traps, following the ideas of Smith[7] and Hartman,[8] and a simple square flyer. Despite the additional complications in manufacturing specimens, with side momentum traps and small tolerances, this configuration could not prevent the formation of cross-shaped cracks (see Fig. 12 in Ref. 6).

Through three-dimensional numerical simulations of the dynamic event and the observation of crack patterns in alumina samples, the efficiency of the star-shaped flyer design was confirmed later by Espinosa *et al.*[4] In contrast to the experiments reported by Chang *et al.*,[6] the recovered specimens did not exhibit cross-shaped cracks for pulse durations of about 300 ns and impact velocities up to 100 m/s. However, a highly cracked ceramic was observed on a ring connecting the inner corners of the star-shaped flyer. Based on three-dimensional calculations, Espinosa *et al.*[4] attributed this damage to spherical release waves emanating from the flyer corners.

More recently, wave trapping in the direction of wave propagation was extended to compression-shear experiments.[9–18] A multiplate flyer with a fluid lubricant was used by Yadav *et al.* and Machcha and Nemat-Nasser, whereas a thin solid polymer layer, easy to manufacture, was used by Espinosa and colleagues.

Mitigation of lateral release waves in compression-shear experiments was extensively investigated by Machcha and Nemat-Nasser.[13] Their results show that usage of the Kumar and Clifton concept results in lower tensile stresses within the specimen central region. Two types of star-shaped geometries and a square plate rotated 45 deg were investigated. However, the investigated multiplate flyer geometries made use of the star-shaped geometry on the second plate rather than the first plate. Moreover, Machcha and Nemat-Nasser conducted experiments only on round samples at impact velocities around or below 100 m/s. The ceramic samples were not recovered intact but rather as large fragments. However, cross-shaped cracks were observed when circular plates were employed for the first flyer plate, sample plate and back plates, and square plates were used as the second plate in multiplate flyers.

We address the difficult problem of recovery of brittle specimens subjected to axial and shear stresses high enough to initiate damage but not necessarily leading to catastrophic failure. Typically, shear stresses of a few GPa are needed for initiating damage in confined brittle material such as Al_2O_3,

H. D. Espinosa is an Associate Professor, A. Patanella is a Graduate Student and Y. Xu is a Graduate Student, School of Aeronautics and Astronautics, Purdue University, West Lafayette, IN 47907.

Original manuscript submitted: February 18, 1999.
Final manuscript received: May 11, 2000.

SiC and TiB_2. In this work, impact velocities between 100 m/s and 200 m/s are selected to achieve this goal. The upper limit is approximately twice as high as the impact velocities reported in the literature in similar studies. We also examine the use of the star-shaped flyer as a first plate in the multiplate flyer design. The response of square and round ceramic specimens is also investigated. In the latest case, a confining plate with a square shape is utilized.

Pressure-shear Recovery Experiments

Plate impact experiments offer unique capabilities for the mechanical characterization of advanced materials under dynamic loading conditions.[3] These experiments allow high stresses, high pressures, high strain rates and finite deformations to be generated under well-characterized conditions. The testing techniques can be divided into two categories: (a) stress wave propagation tests (compression-shear impact and normal impact) and (b) nominally homogeneous deformation tests (high strain rate compression-shear configuration). All rely on the generation of one-dimensional waves in the central region of the specimen to allow a clear interpretation of the experimental results and the mathematical modeling of the material behavior.

Compression-shear loading is attained by inclining the flyer, specimen and target plates with respect to the axis of the projectile.[19] By varying the angle of inclination α, a variety of loading states may be achieved. The experimental setups for high strain rate compression-shear and wave propagation configurations, designed for specimen recovery, are shown in Figs. 1 and 2. Pressure shear recovery experiments offer several advantages over other experimental techniques in the study of damage and inelasticity in advanced materials. The stress amplitudes and deformation rates obtained in these experiments allow the identification of damage and material instabilities. Furthermore, if intact samples are recovered, the information gathered from these experiments can be substantially increased by correlation of real-time velocity profiles and microstructural features associated with mechanisms of inelasticity and damage.

One of the problems of the compression-shear recovery experiment is the simultaneous trapping of the longitudinal and shear waves by a back plate. To solve this problem, the present investigation uses the multiplate flyer discussed in Refs. 10 and 14-17. Such a flyer consists of a thin solid film made of a material with a very low shear flow stress (e.g., a polymer), sandwiched between two thicker hard plates. Due to mismatch in impedances between the thin solid film and the bounding plates, a few reverberations within the polymer film are required to achieve the imposed normal stress at the impact face. This feature imposes another requirement in the design and manufacturing of the thin polymer film. The requirement is that the thickness of the thin film be minimized such that the time required to achieve a homogeneous stress state is only a small fraction of a microsecond. We have manufactured such a multiplate flyer by bonding two hard plates with a uniform 1 μm thick polymer layer (photoresist AZ 1350J-HOECHST CELANESE). We have observed that the uniformity of the thin film prevents tilt between the flyer plates that would otherwise perturb the interferometric measurements. To have a well-defined stress history within the sample, the flyer plate is backed by a low-impedance material and the projectile is stopped by a hard steel anvil.

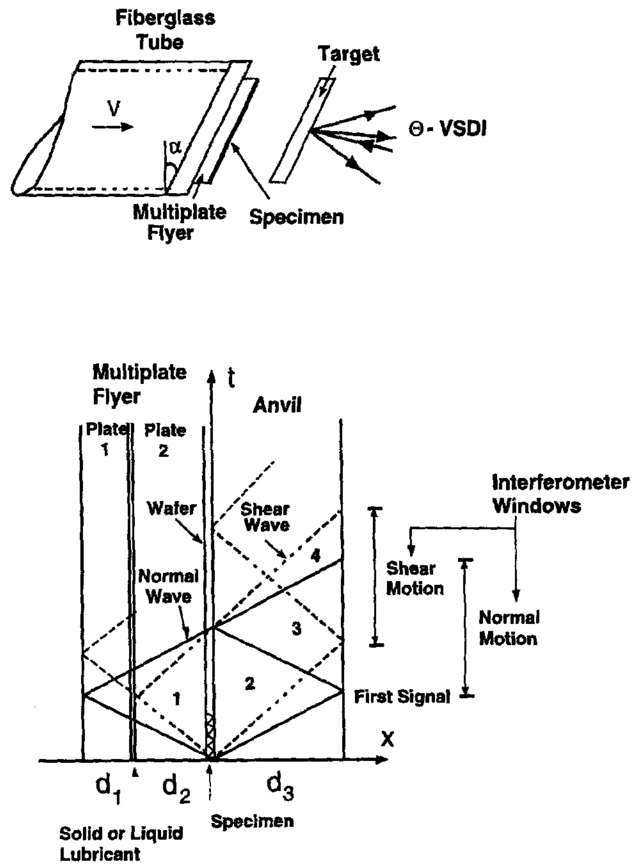

Fig. 1—(a) High strain rate configuration, (b) Lagrangian *X*-*t* diagram of compression-shear high strain rate experiment according to one-dimensional elastic wave theory (VSDI = variable sensitivity displacement interferometer)

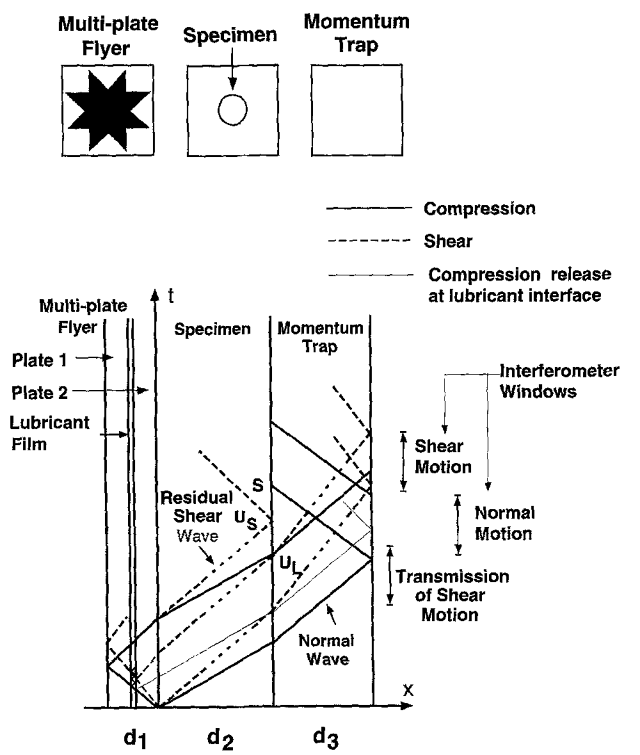

Fig. 2—(a) Wave propagation compression-shear configuration with lateral wave trapping, (b) Lagrangian *X*-*t* diagram of compression-shear wave propagation experiment according to one-dimensional elastic wave theory

As shown in Figs. 1 and 2, two compression-shear configurations were investigated. In the case of compression-shear high strain rate experiments, the specimen is a thin wafer, 100 μm to 500 μm thick, sandwiched between two anvil plates. The multiplate flyer consists of a double plate containing a thin polymer film. The first and second flyer plates have thicknesses d_2 and d_1, respectively (see Fig. 1). The elastic wave fronts for this configuration are given in a Lagrangian X-t diagram in Fig. 1. At impact, plane compression waves and shear waves are produced in both the impactor and the target. Because the shear wave velocity is approximately half the longitudinal wave velocity, a thin film with very low shear resistance needs to be added to the flyer plate such that the arrival of the unloading shear wave to the impact surface precedes the arrival of the unloading longitudinal wave generated at the back surface of the second flyer plate. Certainly, the thickness of the anvil plate must be selected such that the arrival of longitudinal unloading to the impact surface, from the anvil back surface, does not prevent the transfer of the main flyer pulses to the target plate. It should be noted that a residual shear wave remains trapped into the flyer/specimen plates because of the small but finite shear resistance of the thin solid film.

One advantage of this experiment is that it allows the constitutive relation between stress, strain and strain rate to be obtained directly. According to one-dimensional elastic wave theory,[19] the normal stress is given by $\sigma = \rho c_1 u_0/2$, in which ρc_1 is the flyer and anvil longitudinal impedance and u_0 is the normal component of the impact velocity V, that is, $u_0 = V\cos\alpha$. The strain rate is given by the velocity difference between the two faces of the sample divided by its thickness, that is, $\dot{\gamma} = (v_f - v_a)/h = (v_0 - v_{fs})/h$, where v_f and v_a are the flyer and anvil transverse velocities, respectively, at their interfaces with the specimen, and $v_0 = V\sin\alpha$ and v_{fs} are, respectively, the transverse components of the impact velocity and the velocity of the free surface of the anvil plate. The integration of the strain rate over time gives the shear strain $\gamma(t) = \int_0^t \dot{\gamma}dt$. One-dimensional elastic wave theory can be used again to express the shear stress in terms of the measured free surface transverse velocity, that is, $\tau = \rho c_2 v_{fs}/2$, where ρc_2 is the anvil shear impedance. These equations can be used to construct the τ-γ curves at strain rates as high as 1×10^5 s^{-1} and pressures in the range of 2 GPa to 5 GPa.

In the wave propagation compression-shear recovery configuration, the first flyer plate is a star-shaped plate while the second flyer plate could be another star-shaped plate or a square plate. This configuration is shown in Fig. 2. Note that in this figure, the overall thickness of the multiplate flyer is d_1. The specimen thickness is d_2, and the momentum trap thickness is d_3. The elastic wave fronts for this configuration are given in a Lagrangian X-t diagram in Fig. 2. Note at this point that Machcha and Nemat-Nasser positioned the star-shaped flyer as a second flyer plate. Such a design does not exploit the mitigation of lateral release waves, in the central portion of the sample, to its maximum potential. In fact, the impacting front flyer plate has a square shape. Therefore, strong cylindrical release waves are generated from the four plate edges, independent of the star-shaped geometry used in the second flyer plate, for a duration equal to the wave round trip in the first flyer plate.

The selection of plate materials depends on the application for which experiments are conducted. In the characterization of hard materials, demanding requirements are placed on the manufacturing of flyer and momentum trap plates. These plates must be hard enough in compression and shear to remain elastic at the high stress levels required for the inelastic deformation of the specimen, yet strong enough in tension to prevent failure at 45 deg when the shear wave propagates through the unloaded region adjacent to the rear surface of the momentum trap [see Fig. 2(b)]. These requirements are met by using speed-star steel plates with a 0.2 percent offset yield stress greater than 2200 MPa in shear and a tensile strength in excess of 1500 MPa. Another important feature in the selection of the flyer material is that its longitudinal and shear impedances must be smaller or equal to those of the specimen. In this way, a single compression-shear pulse is introduced in the sample. Moreover, the longitudinal and shear impedances of the momentum trap plate must match the impedances of the sample to avoid wave reflections at the specimen-momentum trap interface. Density, wave speeds and impedances for the materials used in this investigation are reported in Table 1.

In the present study, a variable sensitivity displacement interferometer (VSDI)[15,16] is used to monitor both normal and in-plane particle displacements. The system consists of two interferometers working in tandem. A schematic of the optical measuring system is shown in Fig. 3. A diffraction grating is used to produce a normally reflected beam and several diffracted beams. The normally reflected beam is split at beam splitter BS1, and each half of the normal beam is then made to interfere with one of the diffracted beams via beam splitters BS2 and BS3. As a result, a Θ^+ VSDI system and a Θ^- VSDI system are generated. In cases where the surface motion simultaneously exhibits both in-plane and normal displacements, the fringes represent a linear combination of the longitudinal and transverse components of motion. Decoupling of the normal and in-plane displacement histories may be achieved through a linear combination of the two VSDI records. Alternatively, it is always possible to decouple the components of motion by combining a VSDI record with an independent measurement of either component. The VSDI fringe sensitivity is dependent on the angle θ or, equivalently, the frequency σ of the grating manufactured at the observation point and the order n of the diffracted beams.

It is shown in Ref. 16 that the normal and transverse particle motions introduce frequency modulation through the time-varying phase term

$$\Psi^{\pm}(t) = \frac{2\pi}{\lambda}\left[U\left(t - \frac{l}{c}\right)(1 - \cos\theta) \mp V\left(t - \frac{l}{c}\right)\sin\theta\right] + \phi^0 - \phi^{\pm}, \quad (1)$$

where λ is the wavelength of the laser source, l is the initial path length transversed from anvil to detector, c is the speed of light, U and V represent the normal and in-plane displacements of the point of observation from its position at time $t = 0$, and ϕ^0 and $\phi^{\pm}$ are the arbitrary constant phase terms of the reflected and $\theta^{\pm}$ diffracted beams, respectively. Equation (1) shows that each VSDI system will generate a different signal frequency when used to monitor the same given combined state of motion.

Decoupling of the normal motion component $U(t)$ from the in-plane component $V(t)$ is accomplished through one of

TABLE 1—SUMMARY OF MATERIAL PROPERTIES

Material	Density Kg/m^3	c_1 mm/μs	c_2 mm/μs	ρc_1 GPa/mm/μs	ρc_2 GPa/mm/μs
Speed-Star Steel	8138	5.852	3.128	47.62	25.46
TiB_2	4452	10.93	7.3	48.66	32.5
Al_2O_3/SiC	3890	10.56	6.24	41.08	24.27

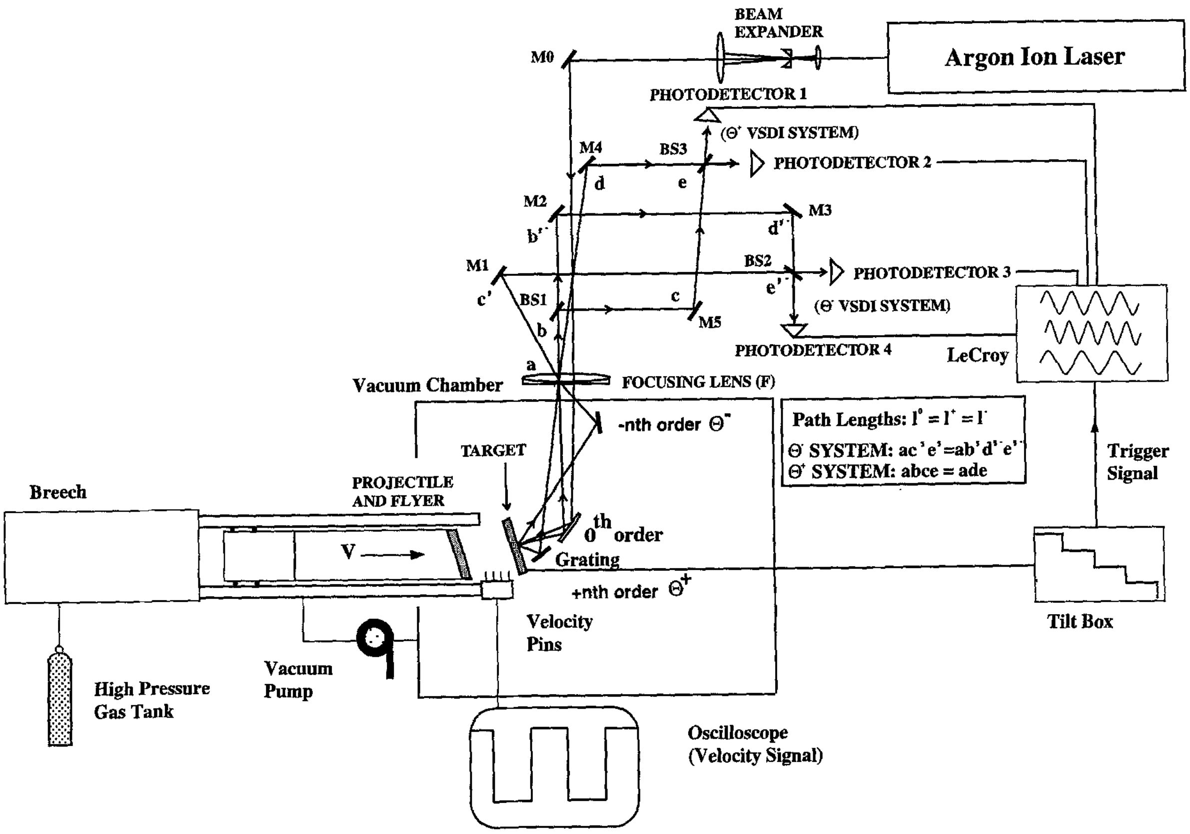

Fig. 3—Optical layout of a variable sensitivity displacement interferometer (VSDI) system. The $\Theta^{\pm}$ VSDI system is obtained by combining a normally reflected beam and a diffracted beam at an angle $\theta^{\pm}$. In this figure, mirrors M0 to M5 and beam splitters BS1 to BS3 are used to obtain the VSDI systems. The lens with focal length F is used to focus the beam at the grating plane in the anvil back surface

the two possible schemes. Both schemes involve the simultaneous application of two interferometers and the use of eq (1) to decouple the two components of motion. In the first scheme, two VSDI systems are employed. The normally reflected beam is split into two beams, one of which interferes with the θ^+ beam to form the Θ^+ VSDI system and a second one that is made to interfere with the θ^- beam to form the Θ^- VSDI system. The two resulting signals may then be linearly combined through the use of eq (1) to solve for longitudinal motion $U(t)$ and transverse motion $V(t)$, respectively. Addition of the phase terms of the Θ^+ and Θ^- VSDI signals provides an expression for a new phase term associated solely with a normal displacement U given by

$$\Psi(t)^+ + \Psi(t)^- = \frac{4\pi}{\lambda} U\left(t - \frac{l}{c}\right)(1 - \cos\theta) + 2\phi_0 - \phi^- - \phi^+. \tag{2}$$

Hence, the fringe constant relation of this new signal is

$$\left[\frac{\text{normal displacement}}{\text{fringe}}\right] = \frac{\lambda}{2(1 - \cos\theta)}. \tag{3}$$

It should be noted that this sensitivity is twice the sensitivity obtained by a single VSDI system for the case of pure normal motion, basically because the signal obtained by addition of the phase terms of the two VSDI systems exhibits a double recording of the normal displacement.

By subtracting the phase terms of the Θ^+ and Θ^- VSDI signals, an expression for a phase term associated solely with an in-plane motion V is obtained, that is,

$$\Psi(t)^- - \Psi(t)^+ = \frac{4\pi}{\lambda} V\left(t - \frac{l}{c}\right)\sin\theta - \phi^- + \phi^+. \tag{4}$$

The fringe constant of this new signal is given by

$$\left[\frac{\text{transverse displacement}}{\text{fringe}}\right] = \frac{\lambda}{2\sin\theta}. \tag{5}$$

This sensitivity is the same as the one exhibited by the transverse displacement interferometer (TDI).[20] This result is not surprising, since the signal obtained by subtracting the phase terms of the two VSDI systems eliminates the effect of the normally reflected beam. We can conclude that this resulting signal is a TDI signal.

In cases where the dual VSDI arrangement is ruled out due to frequency considerations, it is always possible to independently monitor one of the motion components through the simultaneous implementation of an alternative technique. For example, the corresponding transverse displacement history $V(t)$ may be obtained through the employment of a TDI. In this technique, the transverse displacement history is obtained by interfering two symmetrically diffracted laser beams. It was shown by Kim *et al.*[20] that if the path lengths l^+ and l^- of the diffracted beams are kept equal, then the resulting fringe record remains unaffected by the presence of normal motion and is solely a measure of the in-plane displacement. The transverse displacement history $V(t)$ determined in this way can be combined with a VSDI record to decouple the normal displacement $U(t)$ through the use of eq (1). For instance, by subtracting the time-varying phases of a Θ^- VSDI system and a TDI system, we obtain an expression for a phase term associated solely with the normal displacement $U(t)$, namely,

$$2\Psi(t)_{\Theta-\mathrm{VSDI}} - \Psi(t)_{\mathrm{TDI}} = \frac{4\pi}{\lambda} U\left(t - \frac{l}{c}\right)(1 - \cos\theta) + \phi_{\mathrm{TDI}} - \phi_{\Theta-\mathrm{VSDI}}. \quad (6)$$

This equation shows again that the normal motion can be recorded with the sensitivity given by eq (3). The in-plane motion V can be directly obtained from the TDI signal. In eq (6), ϕ_{TDI} and $\phi_{\Theta-VSDI}$ represent the arbitrary constant phases of the TDI and Θ^- VSDI systems, respectively.

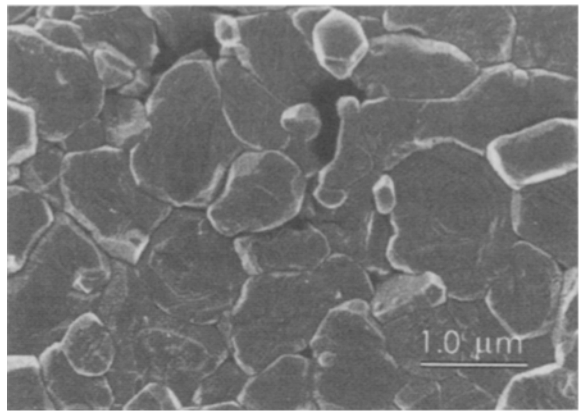

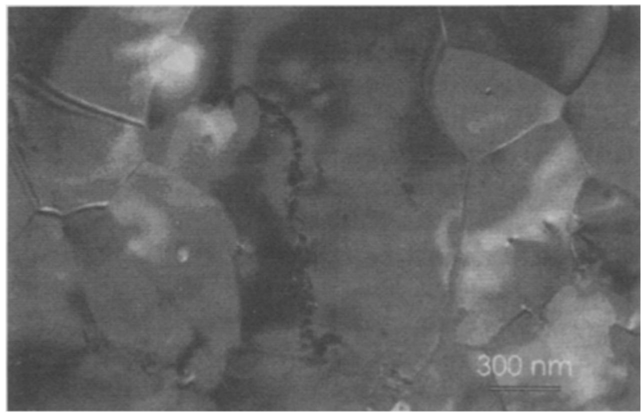

Fig. 4—Scanning electron microscope and transmission electron microscope images of the tested Al_2O_3/SiC nanocomposite

Experimental Procedure

Pressure-shear recovery experiments were carried out in a 3.0 in. gas gun at Purdue University. The multiplate flyer and target plates were made of speed-star steel. The specimens were made with two types of ceramics. In the high strain rate compression-shear experiment, an Al_2O_3/SiC nanocomposite wafer was used. The nanocomposite was manufactured at Purdue University following the technique discussed in Ref. 21. Micrographs of the material microstructure are shown in Figs. 4(a) and 4(b). The Al_2O_3/SiC nanocomposite has an average grain size of 1 µm. Nanosize SiC particles can be observed in the transmission electron microscope image shown in Fig. 4(b). These particles are smaller than 30 nm in size and located within the Al_2O_3 grains and at their grain boundaries. Some SiC particles are large enough to produce dislocations within the grains upon cooling during the sintering process. The material exhibits a flexural strength of about 1 GPa and a macroscopic toughness of about 4 MPa $\sqrt{\mathrm{m}}$.

TiB_2 plates manufactured by CERCOM were employed in the wave propagation compression-shear experiments. Two specimen configurations were investigated. The first consists of a square specimen with the same dimensions as the star-shaped flyer. The second configuration consists of a hollow square steel plate in which a TiB_2 ceramic rod, 12.7 mm in diameter, was shrink fitted. All plates were lapped flat using 15 µm silicon carbide powder slurry. This was done to a flatness better than 3 rings, measured by means of a Newton interferometer.

In the case of high strain rate compression-shear experiments, the specimen was epoxied to a round multiplate flyer. The thin specimen and the multiplate flyer were clamped tightly to avoid penetration of the epoxy into the specimen-flyer interface, and the epoxy was applied around the periphery. A thin layer of aluminum was then vapor deposited on the outer ring of the impact face to provide an electrically conductive surface for measurement of any misalignment between target and flyer at the time of impact.

In the case of wave propagation compression-shear experiments, the thick ceramic specimen was attached to the momentum trap plate by first clamping the plates and then applying a small amount of epoxy at the four corners. In this configuration, tilt was measured by bonding outer aluminum rings to the flyer and target plates.

The impactor was glued to the front end of a fiberglass tube with the impact plane skewed from the axis of the tube at the desired angle. An aluminum piston, with two rubber O-rings, was mounted to the rear end of the fiberglass tube to seal a wraparound breech. A key was also mounted on the middle of the fiberglass tube to prevent rotation of the flyer plate. The whole assembly, back aluminum piston, fiberglass tube and front plate constitute the so-called projectile.

The target rear surface was polished, and then a thin layer of positive photoresist was deposited using a spinning machine. A holographic phase grating was constructed by interference of two laser beams. The angle between the beams was selected such that a sinusoidal profile with 1000 lines/mm was obtained. This grating was used to measure the normal and transverse displacements by means of a VSDI.[16] The signals generated by each interfering beam pair were monitored by silicon photodetectors manufactured by EG&G, with a bandwidth of 800 MHz, in a LeCroy 9384L oscilloscope with 1 GHz bandwidth.

The target plate was mounted in a holder ring and aligned to the face of the projectile to within 0.5 milliradians using the optical technique developed by Kumar and Clifton.[22] To check the angle of misalignment at impact, four copper pins were mounted on the target plate. At impact, these pins come in contact with the deposited aluminum film on the flyer, resulting in four voltage steps in the ratio of 1:2:4:8 that are recorded in a Tektronix TDS 520C oscilloscope. The projectile velocity is measured by recording the times of contact of four wire pins placed in the path of the projectile.

Experimental Results

Three shots were conducted using the experimental configurations discussed earlier. In all three experiments, a skew angle of 18 deg was used. A summary of these experiments is presented in Table 2. Shot 7-1025 was conducted using the high strain rate compression-shear recovery configuration. The specimen was an Al_2O_3/SiC nanocomposite 540 μm thick. Shots 7-1115 and 8-0131 were conducted using the wave propagation compression-shear recovery configuration. In shot 7-1115, the specimen plate consisted of a TiB_2 rod confined by a square steel plate (see Fig. 2). In shot 8-0131, the specimen consisted of a square TiB_2 plate.

The monitored signals in experiment 8-0131 are given in Fig. 5. Decoupling between the normal and in-plane motions is accomplished by first obtaining the in-plane motion, V, directly from the TDI signal and then the normal motion, U, from eq (6). To eliminate electronic noise, the interference fringes are filtered using a fast Fourier transform method with a cutoff frequency higher than the maximum fringe frequency. Furthermore, because the signal amplitude does not contain displacement information, it is customary to scale the signal to a constant amplitude prior to the displacement calculation. Hence, the filtered fringes are scaled to obtain uniform fringe amplitude. If $y_0(t)$ represents the amplitude-corrected signal, a phase function can be obtained as $f(t) = \arcsin(y_0(t))$. Then, the displacement can be computed as $d(t) = d_0 f(t)/2\pi$. The constant d_0 is a function of the interferometer and is defined by eqs (3) and (5) for the VSDI and TDI systems, respectively. Velocities are obtained by differentiating the displacement histories numerically. All the calculations are automatically performed with MATLAB.[23] The functions MENU, GINPUT, INPUT and STRCMP were used to input the data files. The functions FIR1 and FFTFILT were used to perform the fast Fourier transform filtering. The function GRADIENT was used to perform the numerical differentiation.

Normal velocity-time profiles obtained from experiment 7-1025 are shown in Fig. 6. The normal particle velocity shows a velocity reduction after an initial jump indicating the presence of a small gap between the Al_2O_3/SiC nanocomposite and the multiplate flyer. Upon reverberation of waves within the specimen, the normal velocity rises to a value of about 140 m/s at approximately 0.4 μs and remains almost constant until release waves from the boundary reach the observation point. The peak normal stress in this shot, computed according to $\sigma = \rho c_1 u_{fs}/2$, reaches 3.45 GPa.

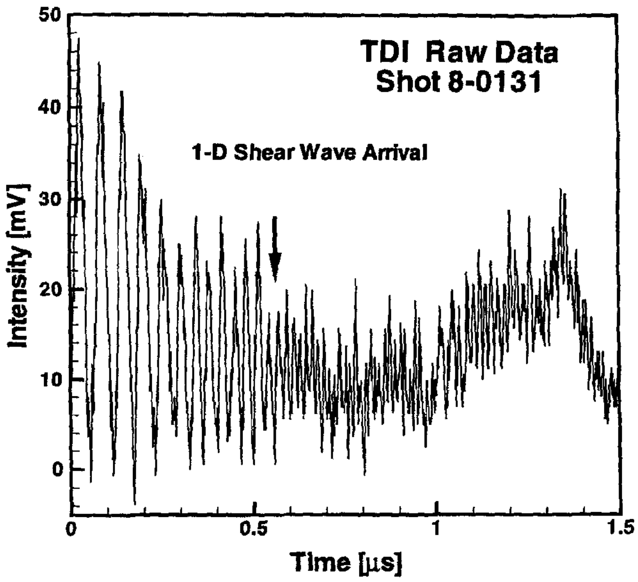

(a)

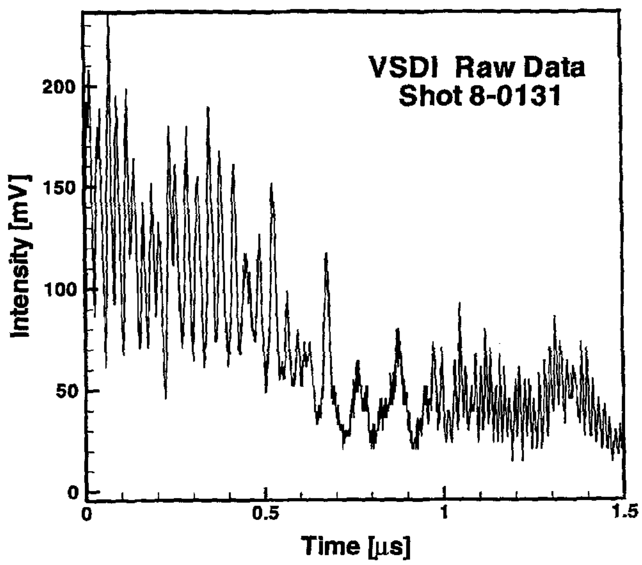

(b)

Fig. 5—(a) LeCroy digital signal from the Θ^- variable sensitivity displacement interferometer (VSDI) (shot 8-0131), (b) digital signal from the transverse displacement interferometer (TDI) (shot 8-0131)

The transverse particle velocity history for experiment 7-1025 is shown in Fig. 7. The velocity rises progressively and then drops for a few nanoseconds. Because in this experiment shear motion is transferred by friction, a reduction in normal traction at the specimen-steel plate interface results in a drop of the transmitted shear motion. When the gap closes, the transverse velocity increases until it reaches a maximum value of 22 m/s at about 500 ns. Then, it decays continuously while the normal velocity remains constant (see Fig. 6). The maximum shear stress, given by $\tau = \rho c_2 v_{fs}/2$, is 280 MPa. This value is well below the expected shear stress of 575 MPa assuming elastic material response. The progressive

TABLE 2—SUMMARY OF COMPRESSION-SHEAR EXPERIMENTS

Shot Number	Specimen/ Thickness [mm]	Flyer Thickness [mm]	Target Thickness [mm]	Projectile Velocity [m/sec]	Tilt [mrad]	Configuration
7-1025	Al_2O_3/SiC/0.54	2.42/3.65	7.99	148	1.3	HSRR*
7-1115	TiB_2/4.15	1.04/2.55	4.53	130	20.3	WPR+
8-0131	TiB_2/8.9	0.92/3.0	4.05	133	1.32	WPR+

HSRR: High Strain Rate Recovery
WPR: Wave Propagation Recovery

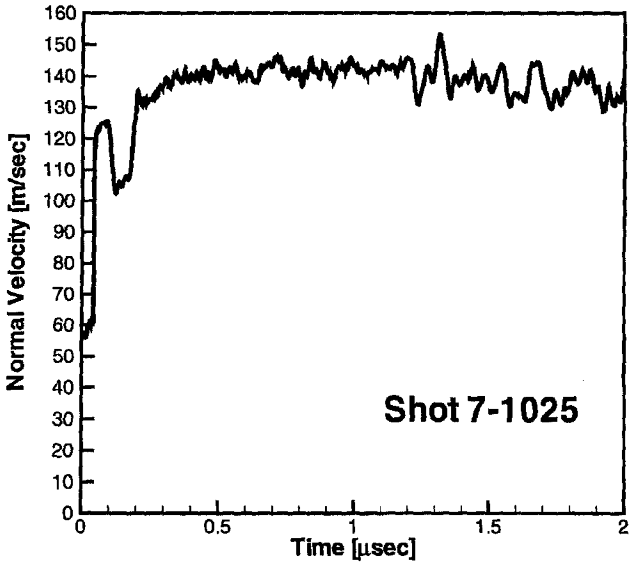

Fig. 6—Normal velocity histories from compression-shear experiment 7-1025. The plotted time is after the arrival of the normal wave to the anvil back surface

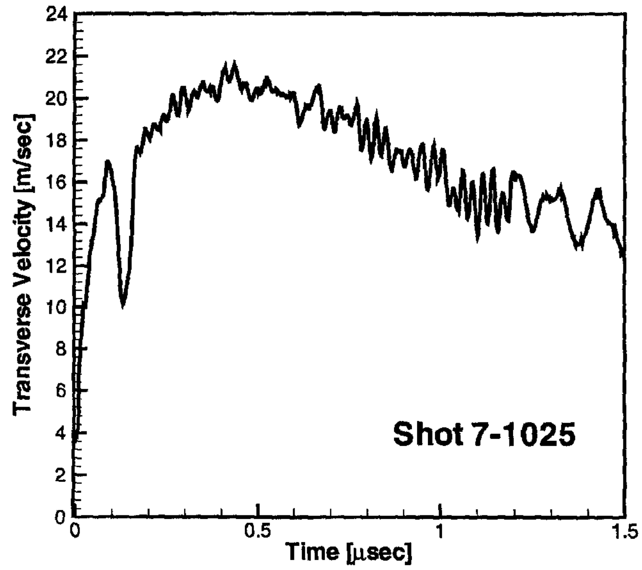

Fig. 7—Transverse velocity histories from compression-shear experiment 7-1025. The plotted time is after the arrival of the shear wave to the anvil back surface

reduction in anvil free surface transverse velocity implies a variable strain rate and absence of a homogeneous stress state in the sample. This feature has been previously observed in materials undergoing damage and inelasticity[5,24] or when frictional sliding occurs.[16] Surface roughness measurements performed after the experiment reveal an *Ra* value of 0.164 μm on the Al_2O_3/SiC nanocomposite and similar values on the steel surfaces. It should be noted that the information obtained experimentally is not sufficient to identify the inelastic mechanisms reflecting the measured velocities. The analyst must also perform numerical simulations of the experiment to gain further insight into the failure mechanisms.[7,10,24–26] This requirement is one of the compelling reasons for attempting specimen recovery in impact experiments. In the present case, round plates are used and the sample is precracked through a sequence of microindentations in a diameter of 1.5 in. Lateral trapping of release waves is attempted by forming a circular crack with the unloaded sample in the central region. Despite all these efforts, the degree of damage is severe enough that the ceramic sample is reduced to fine powder upon unloading. This feature of material pulverization upon unloading was investigated by Zavattieri *et al.*[27] by simulating compression-shear loading on representative volume elements at the grain level. These investigators showed that a ceramic microstructure containing a dilute set of microcracks may pulverize in unloading due to the stored elastic energy within the grains.

To further investigate lateral wave trapping, in addition to wave trapping in the direction of impact, wave propagation experiments were performed on 4 mm to 9 mm thick TiB_2 ceramic samples with either a square shape (31.8 mm × 31.8 mm) or a round shape 12.7 mm in diameter. In the latter case, the specimen was inserted in a speed-star steel square sleeve (31.8 mm × 31.8 mm) by means of shrink fitting.

In experiment 7-1115, the multiplate flyer, the specimen/sleeve and the momentum trap plates were recovered despite the fact that the measured tilt exceeded the allowable tilt for interferometric recording. A magnified photograph of the plates is given in Fig. 8, showing the confining square plate and the TiB_2 specimen together with pieces of the star-shaped flyer plate (left) and the momentum trap plate (right). Several interesting observations can be made. The steel star-shaped flyer is fractured in a pattern that leaves triangular-shaped pieces detached from the central region. Indentation marks, on the steel plate containing the shrink-fitted ceramic, were also observed. The round ceramic sample is partially intact with the back surface spalled. The steel momentum trap plate has cross-shaped cracks with well-defined round indentation at the location where the TiB_2 sample made contact during impact. It should be noted that TiB_2 has longitudinal and shear wave speeds well in excess of steel (see Table 1). Hence, waves arrive at the ceramic-momentum trap interface before they reach the sleeve-momentum trap interface. Moreover, the longitudinal and shear impedances

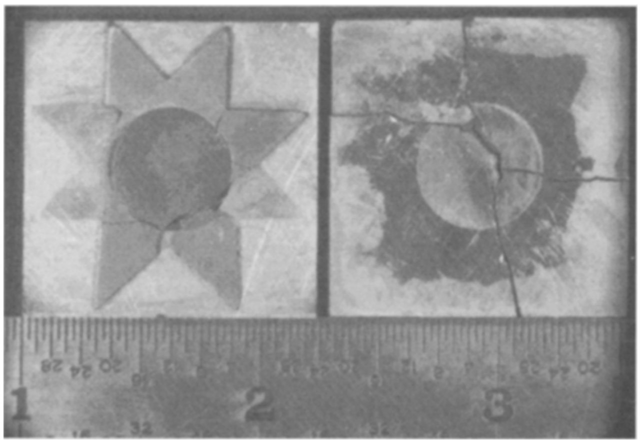

Fig. 8—Optical micrograph of recovered plates from experiment 7-1115

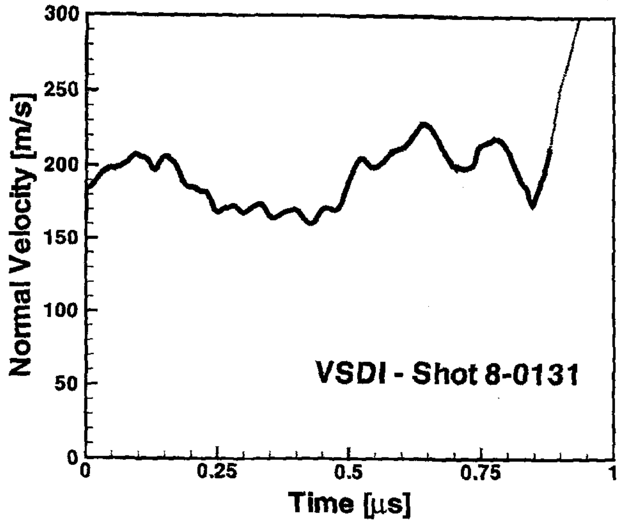

Fig. 9—Normal velocity histories from compression-shear experiment 8-0131. The plotted time is after the wave arrival to the momentum trap back surface (VSDI = variable sensitivity displacement interferometer)

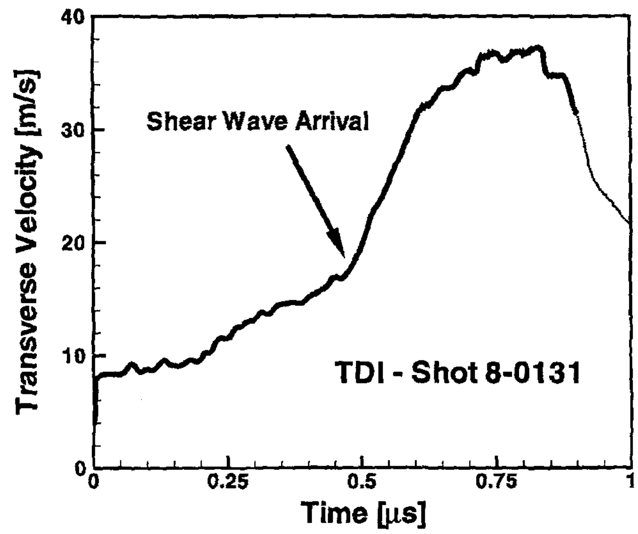

Fig. 10—Transverse velocity histories from compression-shear experiment 8-0131. The plotted time is after the wave arrival to the momentum trap back surface (TDI = transverse displacement interferometer)

of TiB_2 are higher than those of speed-star steel by 2 percent and 27 percent, respectively. These two features contribute to a nonuniform traction, in the contact interface, resulting in bending effects that lead to the observed cross-shaped fragmentation in the momentum trap plate. In fact, such a failure is not observed in the case of a square TiB_2 plate specimen backed by a square momentum trap plate. Based on this understanding and interpretation of the experiment, it was concluded that its repetition was not needed.

In the case of experiment 8-0131 for a square-shaped TiB_2 plate specimen, longitudinal and shear waves were recorded successfully. Plots of normal and transverse particle velocities are shown in Figs. 9 and 10, respectively. The velocity profile in the initial microsecond is shown in solid lines, whereas the remaining part is shown in dashed lines. We make this distinction because during the first microsecond, the signal-to-noise ratio is high enough to give confidence in the measurement. However, at later times the signal to noise deteriorated significantly. This feature is not surprising, since many interfaces are used in this configuration and each one can introduce small rotations of the back surface leading to amplitude variations in the signals.

Figure 9 shows that the normal velocity rises to a value predicted by one-dimensional elastic wave theory. After approximately 200 ns, the longitudinal particle velocity progressively decays and then rises again at about 500 ns. This longitudinal velocity history is very close to the one-dimensional elastic wave propagation prediction if the effect of spherical waves emanating from the star-shaped flyer corners is taken into account.[7] Another source of stress decay is the presence of a thin polymer layer in the multiplate flyer. As previously discussed, longitudinal stress decay occurs until a homogeneous deformation state is reached in the polymer film.

The transverse particle velocity shown in Fig. 10 also presents clear features. Upon wave arrival to the back surface of the momentum trap plate, an in-plane velocity of about 10 m/s is measured interferometrically. After shear wave arrival, according to the *X-t* diagram discussed earlier, the transverse velocity rises to a maximum of 38 m/s. This value is below the shear wave velocity predicted by one-dimensional wave propagation theory. Hence, the material clearly exhibits inelastic behavior in shear. At approximately 800 ns, the transverse velocity decays progressively. Understanding these complex velocity histories (shown in Figs. 9 and 10) requires complete three-dimensional simulations of the compression-shear experiment including damage and tilt effects.

In this experiment, the steel plates were fully recovered. In contrast to the shrink-fitted specimen, the ceramic specimen was fragmented with varying fragment sizes (see Fig. 11). The larger fragment is several millimeters in size, but its location in the square plate could not be identified unambiguously. In this case also, the star-shaped flyer was fragmented in the central region. In addition, long cracks were observed running parallel to the edges. Severe indentation was observed in the second flyer plate, although its hardness was measured to be $Rc = 55$. In this configuration, the momentum trap plate remained intact, with no cracks observable to the naked eye.

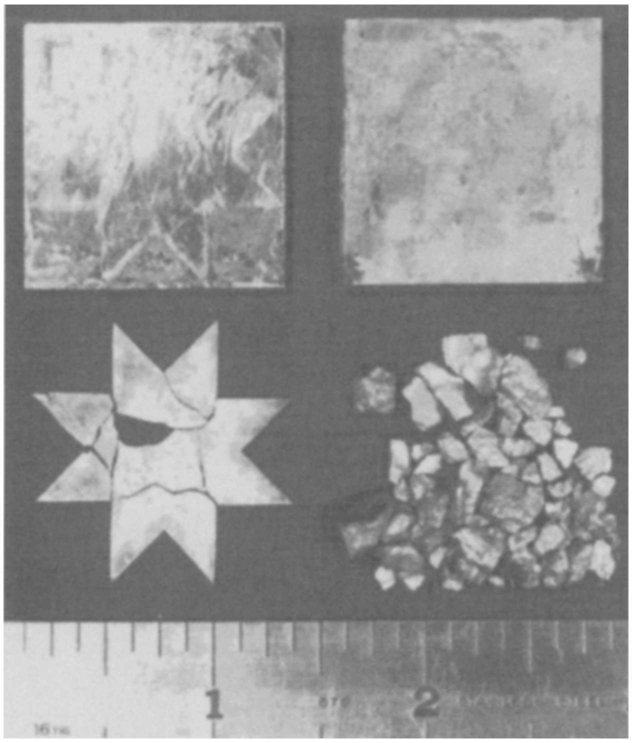

Fig. 11—Optical micrograph of recovered plates from experiment 8-0131. From left to right and top to bottom, note the second flyer plate, the back momentum trap plate, the star-shaped flyer plate and the fragmented specimen

Concluding Remarks

Plate impact compression-shear recovery experiments are presented in which brittle material samples are subjected to a multiaxial dynamic stress state resulting in damage and inelasticity. The velocity profiles of the target surface were measured with a VSDI, yielding normal and transverse velocity-time histories. Several configurations of target plates were investigated to gain insight into plate geometries that can lead to longitudinal and lateral trapping of waves. In all cases, recovery of intact brittle samples was not achieved. It should be noted that brittle materials can pulverize upon unloading if enough damage and elastic energy is stored within the material in the loading phase. Therefore, irrespective of how efficient the wave release is, microcracks grow and coalesce during unloading, resulting in material fragmentation. Numerical simulations of the compression-shear experiment, reported in Ref. 27, show that ceramic pulverization occurs in unloading even in the absence of lateral release waves. The configuration with a multiplate star-shaped flyer and a square plate specimen backed by a square plate momentum trap appears to be the most promising for specimen recovery.

The compression-shear configurations discussed in this paper are expected to be a valuable tool for the investigation of damage and material instabilities in advanced materials. It should be pointed out that the ceramics studied in the present work are susceptible to fragmentation because of their very low toughness and represent the most difficult materials to be investigated in wave propagation experiments with specimen recovery. The compression-shear configurations presented in this work will be more attractive for recovery experiments of other, tougher materials, in which damage, plasticity or phase transformation induced by lateral wave release is reduced to a minimum.

Due to the impossibility of recovering intact brittle materials, when stresses high enough to initiate damage are applied, uncertainties about the site of damage initiation still remains. As previously mentioned, the observed transverse velocity histories could be the result of frictional damage and/or bulk material damage. At the present time, full numerical simulations at the grain size level with models accounting for grain boundary fracture, grain plasticity and interface contact seem to be the only avenue to further investigate the initiation and evolution of damage in brittle materials.

Acknowledgments

The authors would like to thank K. Niihara for sharing his expertise in the preparation of the Al_2O_3/SiC nanocomposites and K. Bowman for making available a hot-pressing capability. Thanks are also due to M. Fischer and H. Arrieta for their help in conducting the compression-shear experiments. The authors acknowledge the support provided by the Army Research Office through ARO-MURI Award No. DAAH04-96-1-0331, the Air Force Office of Scientific Research through Award No. F49620-98-1-0039, the National Science Foundation through Career Award No. CMS-9624364 and the Office of Naval Research YIP through Award No. N00014-97-1-0550.

References

1. *Kumar, P. and Clifton, R.J., "A Star-shaped Flyer for Plate-impact Recovery Experiments," J. Appl. Physics,* **48**, *4850 (1977).*

2. *Raiser, G.F., Clifton, R.J., and Ortiz, M., "A Soft-recovery Plate Impact Experiment for Studying Microcracking in Ceramics," Mech. Mat..* **10**, *43 (1990).*

3. *Espinosa, H.D. and Clifton, R.J., "Plate Impact Experiments for Investigating Inelastic Deformation and Damage of Advanced Materials," Experiments in Micromechanics of Failure Resistant Materials, K.-S. Kim, ed.,* **AMD-130**, *ASME, 37–56 (1991).*

4. *Espinosa, H.D., Raiser, G., Clifton, R.J., and Ortiz, M., "Experimental Observations and Numerical Modeling of Inelasticity in Dynamically Loaded Ceramics," J. Hard Mat.,* **3**, *285–313 (1992).*

5. *Espinosa, H.D., Raiser, G., Clifton, R.J., and Ortiz, M., "Performance of Star Shaped Flyer in the Study of Brittle Materials: Three Dimensional Computer Simulations and Experimental Observations," J. Appl. Physics,* **72**, *3451–3457 (1992).*

6. *Chang, S.N., Chung, D.T., Ravichandran, G., and Nemat-Nasser, S., "Plate Impact Experiments on Mg-PSZ and Improved Target Configuration," Proceedings of the 1989 APS Conference on Shock Compression of Condensed Matter, 389–392 (1990).*

7. *Smith, J.H., "Symposium on Dynamic Behavior of Materials," ASTM Special Technical Publication 336, American Society for Testing and Materials, Philadelphia (1963).*

8. *Hartman, W.F., "Determination of Unloading Behavior of Uniaxially Strained 6061-T6 Aluminum from Residual Strain Measurements," J. Appl. Physics,* **35**, *2090 (1964).*

9. *Ramesh, K.T., unpublished raw data, Army Research Office.*

10. *Espinosa, H.D., "Micromechanics of the Dynamic Response of Ceramics and Ceramic Composites," Ph.D. thesis, Brown University (1992).*

11. *Yadav, S., Davis, J.A., and Ramesh, K.T., "Damage and Recovery Experiments Using Pressure-shear Plate Impact," Experimental Techniques in the Dynamics of Deformable Solids,* **AMD-165**, *71–78 (1993).*

12. *Machcha, A.R. and Nemat-Nasser, S., "Pressure-shear Recovery Experiments," Mech. Mat.,* **18**, *49–53 (1994).*

13. *Machcha, A.R. and Nemat-Nasser, S., "Effects of Geometry in Pressure-shear and Normal Plate Impact Experiments: Three-dimensional Finite Element Simulations and Experimental Observations," J. Appl. Physics,* **80**, *3267–3274 (1996).*

14. *Espinosa, H.D., "Dynamic Compression Shear Loading with In-material Interferometric Measurements," Rev. Sci. Instrum.,* **67**, *3931–3939 (1996).*

15. Espinosa, H.D., Mello, M., and Xu, Y., "A Desensitized Displacement Interferometer Applied to Impact Recovery Experiments," J. Appl. Physics Lett., **69**, 3161-3163 (1996).

16. Espinosa, H.D., Mello, M., and Xu, Y., "A Variable Sensitivity Displacement Interferometer with Application to Wave Propagation Experiments," J. Appl. Mech., **64**, 123–131 (1997).

17. Espinosa, H.D., Xu, Y., and Lu, H.-C., "Inelastic Behavior of Fiber Composites Subjected to Out-of-plane High Strain Rate Shearing," Acta Mat., **45**, 4855–4865 (1997).

18. Espinosa, H.D., Patanella, A., and Xu, Y., "Dynamic Compression-shear Loading of Brittle Materials with Specimen Recovery," Experimental Mechanics, Advances in Design, Testing and Analysis, Proceedings of the 11th International Conference on Experimental Mechanics, edited by I.M. Allison, A. A. Balkema, Rotterdam, 223–229 (1998).

19. Clifton, R.J. and Klopp, R.W., "Pressure-shear Plate Impact Testing," Metals Handbook: Mechanical Testing, **8**, 9th ed., American Society for Metals International, 230 (1985).

20. Kim, K.S., Clifton, R.J., and Kumar, P., "A Combined Normal and Transverse Displacement Interferometer with an Application to Impact of Y-cut Quartz," J. Appl. Physics, **48**, 4132–4139 (1977).

21. Xu, Y., Nakahira, A., and Niihara, K., "Preparation of Al_2O_3/SiC Nanocomposites by Sol-gel Processing," Jap. J. Ceram. Soc., **102** (1994).

22. Kumar, P. and Clifton, R.J., "Optical Alignment of Impact Faces for Plate Impact Experiments," J. Appl. Physics, **48**, 1366–1367 (1977).

23. MATLAB, 1994 User's Guide, MathWork, Natick, Massachusetts (1994).

24. Sundaram, S. and Clifton, R.J., "Pressure-shear Impact Investigation of the Dynamic Response of Ceramics," ASME Special Technical Publication, **AMD-219**, Advances in Failure Mechanisms in Brittle Materials, R.J. Clifton and H.D. Espinosa, eds., Atlanta, Georgia, 59–80 (1996).

25. Espinosa, H.D., Zavattieri, P.D., and Emore, G.L., "Adaptive FEM Computation of Geometric and Material Nonlinearities with Application to Brittle Failure," Mech. Mat., **29**, 275–305 (1998).

26. Espinosa, H.D., Zavattieri, P.D., and Dwivedi, S., "A Finite Deformation Continuum/Discrete Model for the Description of Fragmentation and Damage in Brittle Materials," J. Mech. Physics Solids, **46**, 1909–1942 (1998).

27. Zavattieri, P.D., Raghuram, P.V., and Espinosa, H.D., "A Computational Model of Ceramic Microstructures Subjected to Multi-axial Dynamic Loading," J. Mech. Physics Solids (forthcoming).